Materials Today Bio 24 (2024) 100878

Contents lists available at ScienceDirect

Materials Today Bio

journal homepage: www.journals.elsevier.com/materials-today-bio

Fabricating the multibranch carboxyl-modified cellulose for hemorrhage control

Shengyu Li [a,*,1], Lihong Gong [b,1], Jianglin Chen [c], Xijin Wu [a], Xia Liu [a], Huiying Fu [a,**,1], Qiyang Shou [a,d,***,1]

[a] The Second Affiliated Hospital & Second Clinical Medical School, Zhejiang Chinese Medical University, Hangzhou, 310053, China
[b] Third Clinical Medical School of Zhejiang Chinese Medical University, Hangzhou, 310000, China
[c] School of Pharmaceutical Sciences, Zhejiang Chinese Medical University, Hangzhou, 311402, China
[d] Jinghua Academy, Zhejiang Chinese Medicine University, Jinghua, 321000, China

ARTICLE INFO

Keywords:
Microcrystalline cellulose
Multibranch
Biocompatibility
Hemorrhage control

ABSTRACT

Excessive bleeding is associated with a high mortality risk. In this study, citric acid and ascorbic acid were sequentially modified on the surface of microcrystalline cellulose (MCAA) to increase its carboxyl content, and their potential as hemostatic materials was investigated. The MCAA exhibited a carboxylic group content of 9.52 %, higher than that of citric acid grafted microcrystalline cellulose (MCA) at 4.6 %. Carboxyl functionalization of microcrystalline cellulose surfaces not only plays a fundamental role in the structure of composite materials but also aids in the absorption of plasma and stimulation of platelets. Fourier -transform infrared (FT-IR), thermogravimetric analysis (TGA) and X-ray photoelectron spectroscopy (XPS) spectra confirmed that carboxyl groups were successfully introduced onto the cellulose surface. Physical properties tests indicated that the MCAA possessed higher thermal stability (T_{max} = 472.2 °C) compared to microcrystalline cellulose (MCC). Additionally, in vitro hemocompatibility, cytotoxicity and hemostatic property results demonstrated that MCAA displayed good biocompatibility (hemolysis ratio <1 %), optimal cell compatibility (cell viability exceeded 100 % after 72 h incubation), and impressive hemostatic effect (BCI_{MCAA} = 31.3 %). Based on these findings, the hemostatic effect of covering a wound with MCAA was assessed, revealing enhanced hemostatic properties using MCAA in tail-amputation and liver-injury hemorrhage models. Furthermore, exploration into hemostatic mechanisms revealed that MCAA can significantly accelerate coagulation through rapid platelet aggregation and activation of the clotting cascade. Notably, MCAA showed remarkable biocompatibility and induced minimal skin irritation. In conclusion, the results affirmed that MCAA is a safe and potentially effective hemostatic agent for hemorrhage control.

1. Introduction

On the modern battlefield, 90 % of traumatic injuries involve internal noncompressible bleeding in regions such as joints and trunk, leading to significant prehospital mortalities [1,2]. Moreover, uncontrollable hemorrhage is a primary cause of trauma-related deaths during spinal cord, liver, orthopedic, and surgical procedures [3,4]. Therefore, the urgent development of rapid and effective hemostatic materials is paramount. Currently, the primary materials used for hemostasis include polysaccharide-based materials, inorganic materials, fibrin sealants, and their composites [5–8]. While a variety of hemostatic materials are available in the market, concerns about biocompatibility, hemostatic efficacy, and high cost limit their widespread adoption. For instance, gelatine exhibits slow hemostasis [9], fibrin has a limited shelf life [10], aldehyde cellulose dissolves swiftly [11], thrombin is costly and demands specific storage conditions [12], and the kaolin clay based QuikClot often induces thermal injury and inflammation [13]. Given these limitations, ideal hemostatic materials should offer the benefits of

* Corresponding author.
** Corresponding author.
*** Corresponding author. The Second Affiliated Hospital & Second Clinical Medical School, Zhejiang Chinese Medical University, Hangzhou, 310053, China.
E-mail addresses: 18768393817@163.com (S. Li), fhy131@126.com (H. Fu), sqy133@126.com (Q. Shou).
[1] These authors contributed equally.

https://doi.org/10.1016/j.mtbio.2023.100878
Received 9 August 2023; Received in revised form 16 October 2023; Accepted 20 November 2023
Available online 16 December 2023

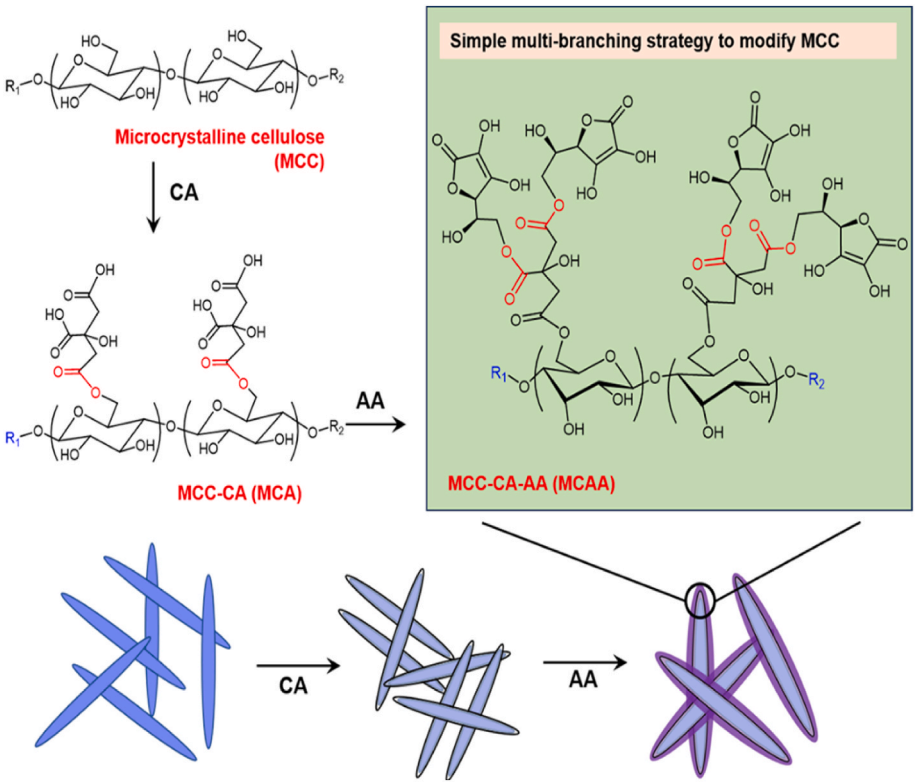

Scheme 1. The schematic preparation of MCA and MCAA.

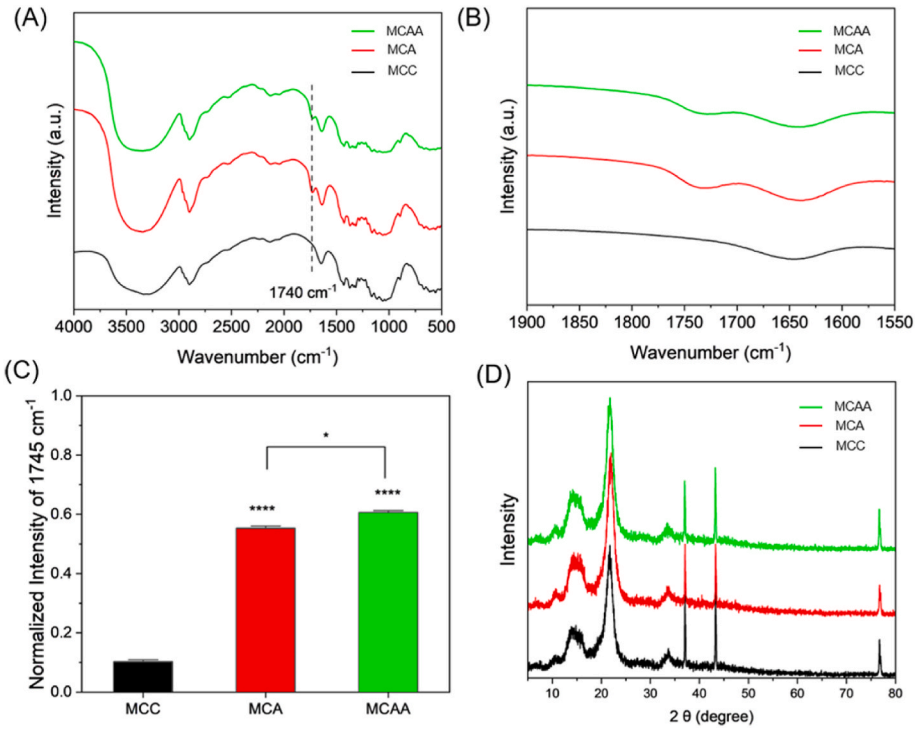

Fig. 1. (A) Characteristic FTIR finger prints of MCC, MCA and MCAA. (B)Characteristic FTIR spectra in the range of 1550–1900 cm^{-1}. (C) Normalized peak intensities of MCC, MCA and MCAA at 1745 cm^{-1}. Statistical analysis was carried out using one-way analysis of variance (ANOVA). (D) Diffractograms of MCC, MCC, MCA and MCAA. Here, the identifiers of all figures are uniform, black for MCC, red represents MCA and green is MCAA.

straightforward preparation, affordability, non-cytotoxicity, and rapid blood loss cessation.

Cellulose nanocrystals showcase numerous outstanding properties, such as high biocompatibility, wound healing capability, adsorption, and biodegradability [14–16]. Concerning the hemostatic properties of cellulose, most studies in the past decade have concentrated on oxidized

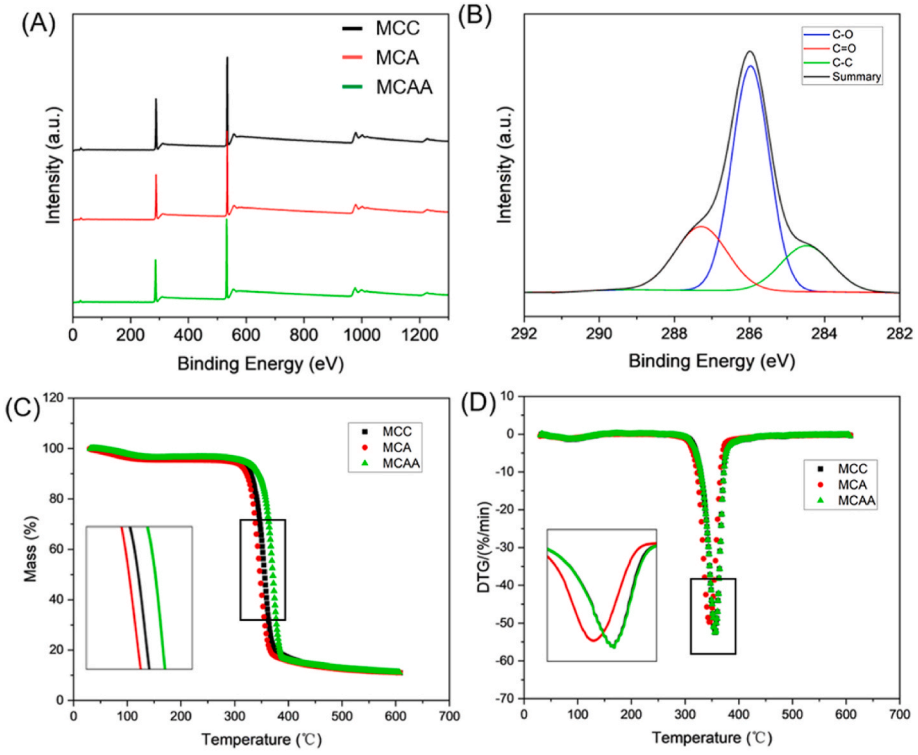

Fig. 2. (A) XPS summary spectra of the MCC, MCA and MCAA. (B) C 1s spectra of MCAA. (C) TGA and (D) DTG curve of the samples.

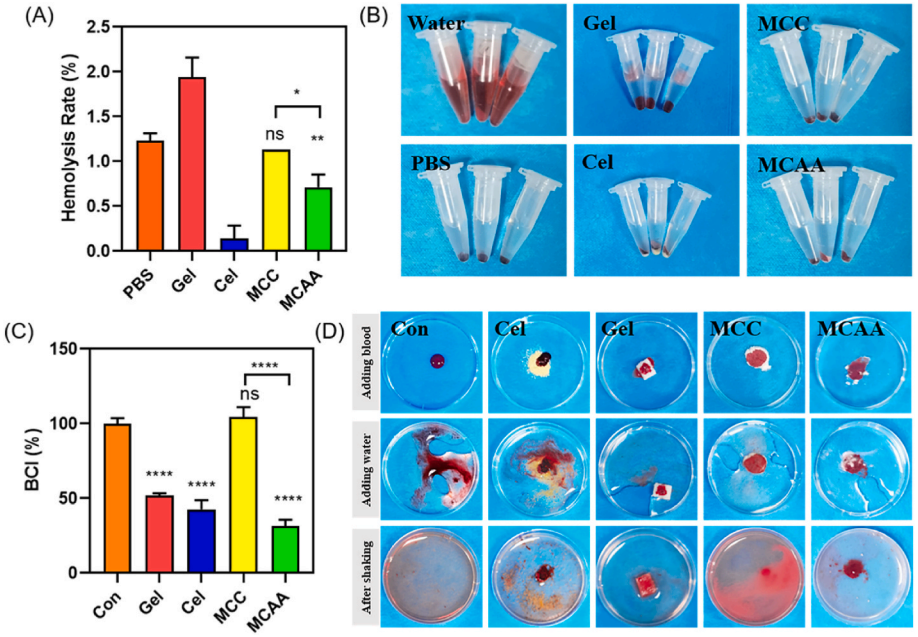

Fig. 3. (A) The hemolysis assay of those samples (Gel, Cel, MCC and MCAA). (B) The images of blood incubated with samples. (C) Quantitative statistics of the blood clotting index, corresponding with various materials. (D) Pictures of the BCI process (n = 5), significance levels of the results compared to the control group were indicated by *P < 0.05, ****P < 0.0001, and using one-way analysis of variance (ANOVA).

cellulose-derived hemostatic agents. These encompass oxidized cellulose, oxidized regenerated cellulose, oxidized regenerated cellulose/chitosan, oxidized microcrystalline cellulose, and oxidized cellulose nanofiber/alginate [9,17–20]. This focus stems from oxidized cellulose's ability to draw fluid from the blood and ensnare proteins, platelets, red blood cells, and other active components [19,21]. For example, a recent study indicated that the carboxyl groups present in oxidized cellulose lowered pH, leading to the nonspecific aggregation of platelets and thrombus generation. Essentially, the carboxyl group could promote the conversion of hemoglobin to acidic heme, release Fe^{3+}, and accelerate thrombosis [22]. Wang posited that carboxyl groups could immediately stimulate erythrocytes and platelets upon blood contact [23]. Huang et al. fashioned carboxyl modified cellulose nanocrystals, revealing that carboxyl groups critically influence the structure and hemostatic features of the composites [24]. Hence, carboxyl groups play an essential role in blood coagulation [25]. However, there is a paucity of research in

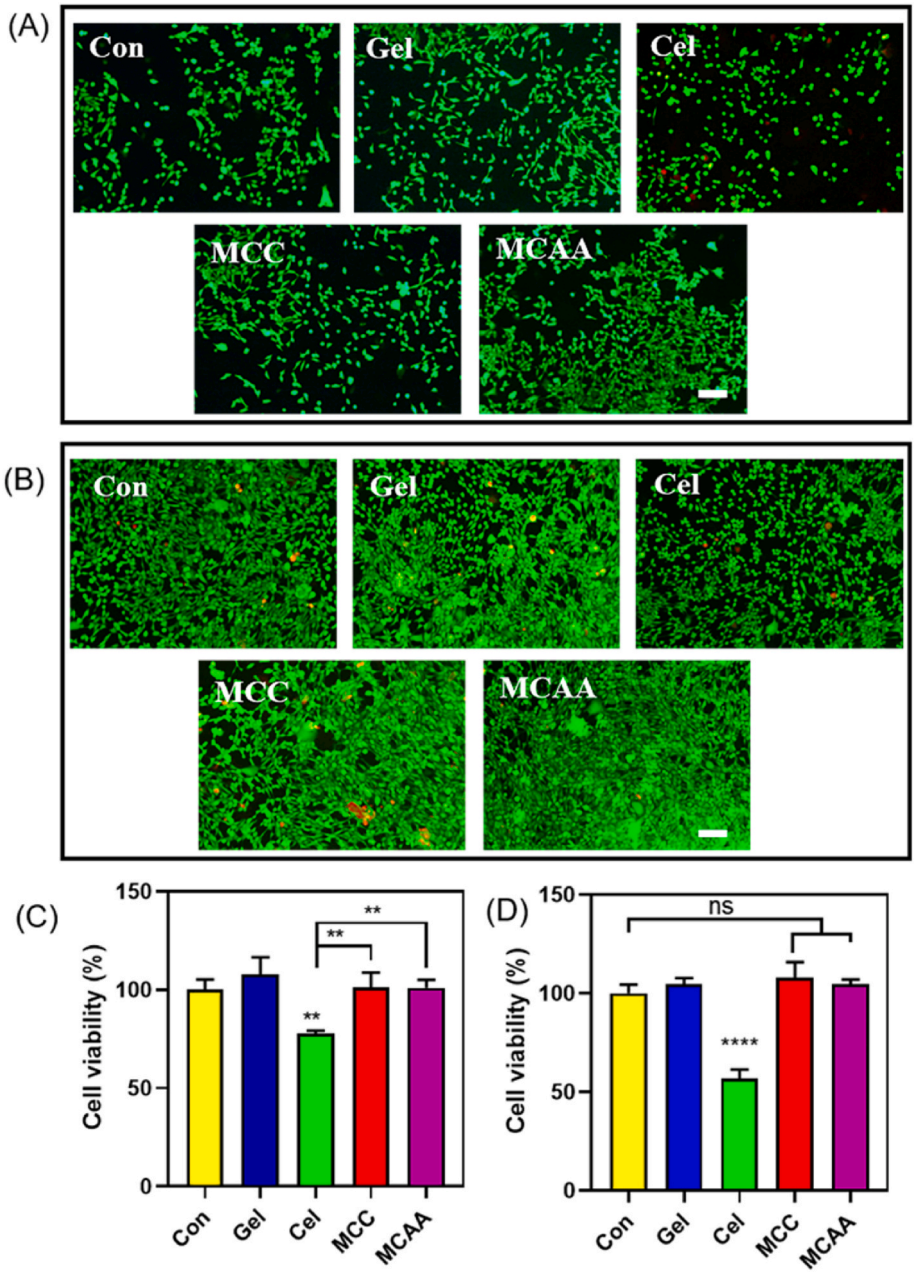

Fig. 4. Staining images of NIH3T3 cells after co-incubate with Gel, Cel, MCC and MCAA for 24 h (A) and 72 h (B). Cell viability of NIH3T3 cells after treatment with samples for 24 h (C) and 72 h (D) Data represent mean ± SD, (n = 4), **p < 0.01 vs control group.

this domain, possibly due to the absence of synthetic methodologies and comprehensive property characterizations to verify increased carboxyl group presence on the cellulose surface.

Carboxylic acid -modified cellulose with charged groups has been effectively created using methods like 2,2,6,6-Tetramethylpiperidine-1-oxyl (TEMPO) radical oxidation [24], ammonium persulfate (APS) oxidation [26], and periodate-chlorite oxidation [27]. Nonetheless, these oxidation techniques come with drawbacks. For instance, TEMPO-mediated oxidation demands prolonged oxidation durations and restricts additional oxidation of the CNC surface. Periodate-chlorite oxidation is costly, harmful, and yields a low carboxyl content. Thus, a straightforward and universal oxidation procedure is essential. In this research, a multi-branch strategy (citric acid/ascorbic acid/-hydrochloric acid hydrolysis) was employed to introduce carboxyl groups onto microcrystalline cellulose (MCC). The hydronium ions (H_3O^+) from HCl or RCOOH disassociation not only hydrolyze MCC's amorphous domains but also facilitate the esterification reaction between MCC's hydroxyl groups and citric acid's carboxyl groups (Scheme 1). Both MCA (MCC modified with citric acid) and MCAA (MCA altered with ascorbic acid) were characterized using techniques such as Fourier transform infrared spectrometry (FT-IR), X-ray diffraction spectrum (EDS), Field Emission Scanning Electron Microscopy (FE-SEM), thermogravimetric analysis (TGA), and X-ray diffraction (XRD). We postulated that this method modifies more terminal functional groups, resulting in elevated carboxyl content on the MCC surface, which could hasten thrombosis. Notably, multi-branch carboxyl modified cellulose can activate both inherent and external physiological coagulation pathways integral to the coagulation process. Additionally, MCAA demonstrated commendable biocompatibility in vivo. This study introduced a ground-breaking cellulose hemostatic material for hemorrhage control, underscoring its potential as a safe and effective hemostatic agent.

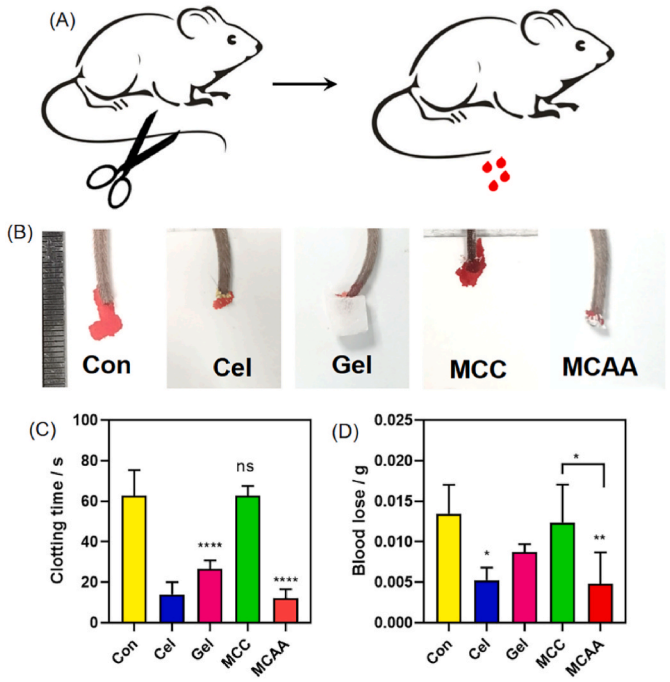

Fig. 5. (A) The schematic diagram of tail-amputation models. (B) Photographs of the tail-amputation models after hemostasis. (C) The bleeding time and (D) blood loss weight of tail-amputation models (n = 5), *P < 0.05, **p < 0.01 vs control group.

2. Experimental section

2.1. Materials

Commercial microcrystalline cellulose (MCC, average particle size 50 μm, DP = 10,000) was purchased from Sinopharm Chemical Reagent Co., Ltd. Citric acid (CC) and ascorbic acid (AC) were purchased from Shanghai Aladdin Bio-Chem Technology Co., LTD. Hydrochloric acid (HCl, 38 %) was provided by Huadong medical Limited by Share, Ltd. Hydrochloric acid was obtained from Zhejiang Chinese Medical University. Activated PT time (aPTT) kit was purchased from Shanghai Yaji Biotechnology Co., LTD. Calcein-AM/Propidium iodide (PI) live/dead kit and Cell Counting Kit-8 (CCK-8) were purchased from Beijing Solaibao Technology Co. LTD. Celox (Cel) was purchased from Qingdao MeiJin R&D Ltd (Qingdao, China). Commercial gelatin hemostatic sponge (Gel) was purchased from Guangzhou Kuai Kang Medical Device Co., LTD. In this work, MCC was selected as positive control while Gel and Cel were negative control. Ultrapure water was used for all experiments (Smart2 pore2, Thermo Scientific Barnstead).

2.2. Preparation of citric-acid-grafted MCC (MCA)

MCA was fabricated as previously reports with some modifications [28]. The MCA were hydrolyzed by 10 % hydrochloric acid (6 M)/90 % citric acid (3 M) (v/v) with mechanical stirring and 80 °C in a 50 mL flask. Subsequently, the suspension was washed repeatedly by centrifugation with deionized water until its pH approached 7. Finally, the MCA was obtained by lyophilization for 2 days.

2.3. Preparation of ascorbic-acid-grafted MCA (MCAA)

The reaction process of MCA graft with ascorbic acid (Scheme 1) is described as follows: MCAA were fabricated by grafting and polymerizing the hydroxyl group of MCAs (3g) and the carboxyl group of CA (9g) with the addition of 10 % hydrochloric acid (6 M). Stirring suspension (1000 rpm) at 80 °C for 4 h. Subsequently, the suspension was washed for 5 times until its pH reached 7.

2.4. Characterization

The morphology of MCC, MCA and MCAA were examined by a Field Emission Scanning Electron Microscopy (FE-SEM, SU8010, Hitachi Limited, Japan) at an acceleration voltage of 2 kV.

Infrared spectrum was taken by using a FT-IR spectrometer under the absorption mode (Thermo Fisher Nicolet iS50), and analyzed a spectral width of 4000 cm^{-1} - 400 cm^{-1}. Besides, the KBr powder was selected as background.

X-ray photoelectron spectroscopy (XPS) was taken by a Kα instrument (Thermo Scientific K-Alpha) with a 1 eV of energy step and 100 eV pass energy.

X-ray Diffraction (XRD) investigations of the as-prepared samples were performed by a Shimadzu XRD-7000X-ray diffractometer with a monochromatic Cu-Kα (λ = 0.15406 nm) in the range of 5°–80°. The details of settings as follows: X-ray generates at 40 kV and 30 mA; scan speeds to be 4.0 (deg/min); divergence slit and scatter slit were selected 1.0°. The crystallinity and average crystallite sizes of such materials were calculated by the following equation [29,30]:

$$X_{crystallinity} = \left[\frac{Ic - Ia}{Ic}\right]$$

Herein, Ic and Ia are the peak intensity at 2θ = 22.7° and 2θ = 18–19°.

In addition, the crystal dimensions of different planes of the materials were calculated by the following equation [28,31]:

$$Dhk = \left[\frac{K\lambda}{B\not{k}\cos\theta}\right]$$

where D_{hkl} is the crystalline dimension of the hk crystal planes; K = 0.94; λ = 1.5406 Å; and B_{hk} is the full width at half-maximum (FWHM) of the reflection peak at the corresponding peak angle θ of the corresponding crystal plane.

Thermogravimetric analysis (TGA, TA-Q600) was carried out test on the samples. The details of settings as follows: under N_2 atmosphere, thermal stability in the range of 30 °C–610 °C; heating rate of 20 °C/min. And the activation energy (Ea) was calculated by analyzing the TGA results [32,33].

$$\ln\left[\ln\left(\frac{w0}{wt}\right)\right] = \frac{Ea * \theta}{R * Ts^2}$$

where, W0 and Wt are the initial weight and the residual weight of the samples at temperature T; R is the gas constant; Ts is the temperature determined at 43.601 % weight loss; θ is T - Ts.

The carboxyl content was mainly based on Boehm titration method [34]. According to which, the carboxyl groups on the surface of the carbon material were only react with $NaHCO_3$ to form carbon dioxide and water. The samples (200 mg) were immersed in 100 mL $NaHCO_3$ solution (0.01 M). After 20 h of stirring, the solution was collected. Then, the solution was titrated with hydrochloric acid (0.01 M). The carboxyl content of such materials was calculated by the following equation:

$$\%\ P_{COOH} = \frac{45 * (M1 - M2) * V3}{W} * 100\ \%$$

where, M1 and M2 are the concentration of $NaHCO_3$, which was titrated by HCl before and after; W is the initial mass of samples; V3 is the initial volume of the $NaHCO_3$.

2.5. Blood Clot Index (BCI)

Blood Clot Index (BCI) is an important index to evaluate hemostatic

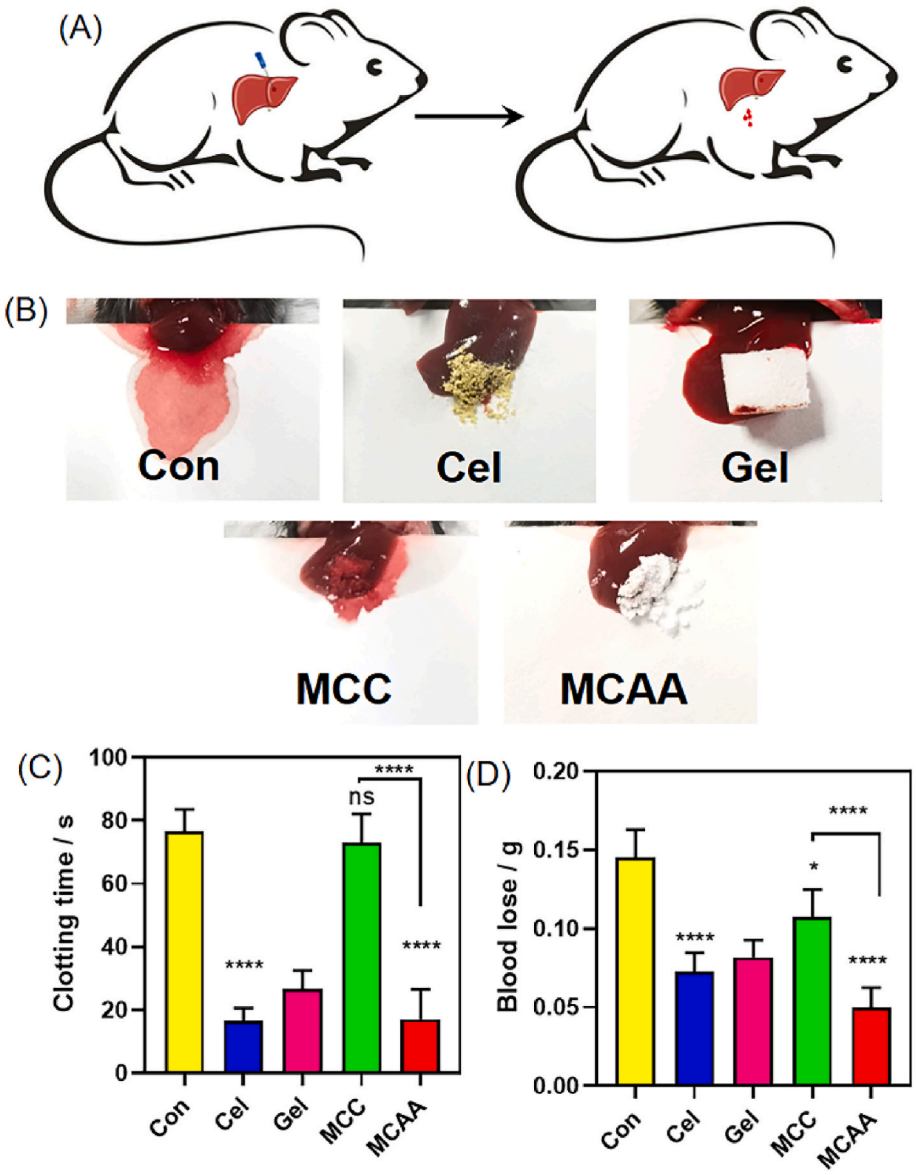

Fig. 6. (A) The schematic diagram of liver-injury models. (B) Photographs of the liver models after hemostasis. (C) The hemostasis time and (D) blood loss of in the model of liver injury. (n = 5), *P < 0.05, **p < 0.01 vs control group.

effect, herein, BCI was calculated as previously reports [35,36]. Whole blood of healthy male SD rats was collected and first added into citrate solution (1:9) to obtain required anticoagulant whole blood. 100 μL of anticoagulant blood was dropped on the surface of samples. The 5 mL of water were added to samples after shaking in a rocking shaker at room temperature for 5 min. The absorbance of the solution at 450 nm to get BCI by a microplate reader (BioTek Cytation 1, Agilent). The BCI was evaluated as the following formula:

$$\mathrm{BCI} = \frac{\mathrm{OD\ (sample)}}{\mathrm{OD\ (\ control)}} * 100\%$$

2.6. Blood compatibility assay

Hemolysis rate is an important index to evaluate blood compatibility [37]. Firstly, the anticoagulant blood (25 μL) was diluted by 1 mL PBS for further use. Then, samples (50 mg) were mixed with the suspension, and incubating at 37 °C for 2 h (for positive control, blood was mixed with 1 mL of water). After centrifugation (3000 r, 15 min), the absorbance of the hemoglobin was measured at 540 nm by an UV–vis spectrometer. And the hemolysis rate was calculated as follows:

$$\text{Hemolysis rate } (\%) = \frac{\mathrm{OD}_{\text{ sample}} - \text{ OD Negative cotrol}}{\text{OD positive }_{\text{control}} - \text{ODNatetive cotrol}} * 100\ \%$$

2.7. aPTT and PT

Anticoagulant whole blood was first separated (3000 rpm, 15 min) to obtain the platelet-poor plasma (PPP). For the aPTT test, the samples were mixed with 100 μL of PPP and aPTT reagent at 37 °C for 3 min. Then, $CaCl_2$ solution was sequentially added into above mixtures to record the appearance time of fibrin filaments. For PT test, the operations were the same as the aPTT test except the reagent and $CaCl_2$ solution [35,38].

2.8. Thrombin assay

Thrombin-antithrombin complex (TAT) was commonly used to analyze indicators of thrombin formation over time [39]. Samples were first mixed with 100 μL of anticoagulant blood at 37 °C for 15 min. After

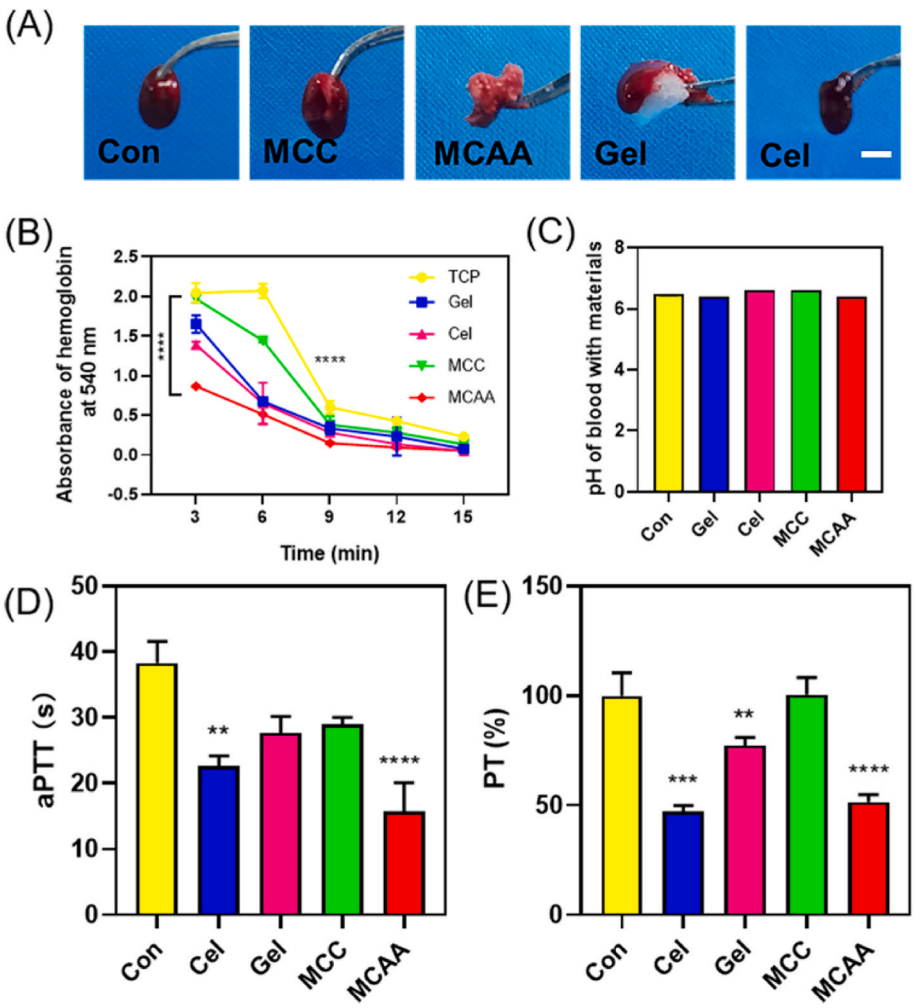

Fig. 7. (A) The photographs of thrombus on material surfaces. Scar bar = 0.2 cm(B) The whole blood clotting kinetics after co-culture with samples. (n = 3), ****p < 0.0001 for MCAA vs TCP. (C) The pH of the solution the thrombus and the material were soaked in water for 24 h. (D, E) Changes in activated partial thromboplastin time (aPTT) and prothrombin time (PT) for plasma with samples.

that, sodium citrate was adding to the solution. The levels of TAT were measured as the instruction of manufacturer.

2.9. Whole blood clotting kinetics

The whole blood clotting capability was performed as previously reports with some modifications [20]. Prior to experiment, activated blood was first prepared by mixing 1 mL 0.1 M $CaCl_2$ with 10 mL citrated blood. Then, 40–50 mg of samples (MCC, MCAA, Gel, Cel and TCP) were added to 24 well plates (n = 5). And the activated blood (200 μL) was added to the surfaces of samples. Subsequently, water (3 mL) was put into each well at every different time (3, 6, 9, 12 and 15min) point. 5 min later, the thrombosis (100 μL, n = 3) were photographed and recorded the absorbance of solution at 450 nm. Besides, the thrombus solidified on the materials was soaked in water (3 mL) for 24 h to measure their solution pH.

2.10. Platelet adhesion

Anticoagulant whole blood was first separated (800 rpm, 15 min) to obtain the platelet-rich plasma (PRP). Samples (Cel, Gel, MCC, and MCAA) were placed into 24-well plates incubated with 100 μL of PRP at 37 °C for 1h. The unattached platelets were gently rinsed three times by PBS. Then, the platelets were lysed by 0.1mL 1% Triton X-100 at 37°C. The lactate dehydrogenase (LDH) enzyme was evaluated by LDH kit (Biyuntian, China) as the instructions of manufacturer and performed at 450nm (Cyatation1, BioTek).

2.11. Biocompatibility

Here, cck-8 assay was conducted to evaluate the in vitro cytotoxicity of the MCAA against mouse fibroblast cells (NIH 3T3). The samples were sterilized by UV for 1 h, then the samples were soaked in medium for 1 day. Prior to performing the assay, leach liquor was obtained by 0.22 μm microporous membrane. NIH 3T3 cells were cultured in 100 μL of leach liquor with a density of 1000 cells/mL, and incubated for 24 h and 72 h. After that, cck-8 assay was performed according to the kit instructions. The cell viability was calculated by the following equation:

$$\text{Cell viability} = \frac{\text{OD}_{\text{sample}} - \text{OD}_{\text{blank}}}{\text{OD}_{\text{control}} - \text{OD}_{\text{blank}}} * 100\%$$

For the live/dead staining test, the cells (5000 cells/mL) were seeded into 24/well plate with incubation for 24 and 72 h. After that, the cells were stained according to the manufacturer's protocol, and cells were observed using a fluorescence microscope (ECLIPSE TI-S, Nikon, Japan).

2.12. In vivo hemostasis and biocompatibility

All animals (weight 20g–25g, SPF grade, C57BL/6 male mice) were supplied by the Zhejiang Chinese Medicine University Laboratory

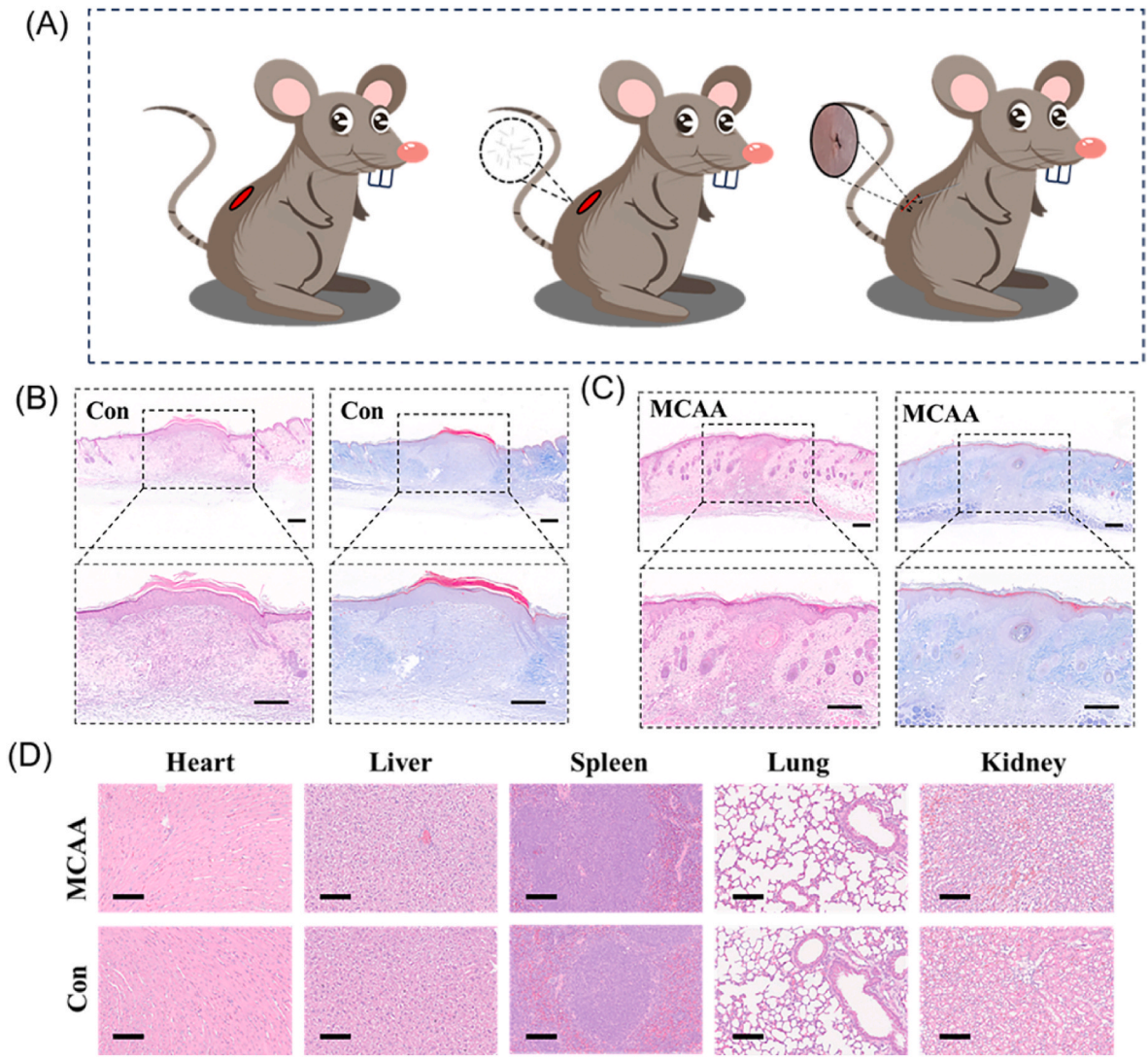

Fig. 8. (A) The process of explants implanted subcutaneously in mice. (B, C) The hematoxylin and eosin (H&E) staining and Masson's trichrome staining (MTS) of MCAA. Scale bars = 200 μm. (D) (H&E) staining of major organs (heart, liver, spleen, lung and kidney). Scale bars = 100 μm.

Animal Research Center and raised at 25 ± 1 °C and 60 ± 10 % humidity before experiment. All of the animal experiments procedure were performed in strict compliance with the National Research Council's Guide for the Care and Use of Laboratory Animals and approved by Experimental Animal Management and Ethics Committee of Zhejiang Chinese Medicine University, Zhejiang, China (ACUC-20220808-01). In our study, we selected C57BL/6 male mice to avoid interference with the female estrus cycle.

The liver-injury model can refer to previous study as an in vivo irregular and deep wound [2]. The 0.3 % pentobarbital sodium anesthesia was first injected into the abdominal cavity of C57/BL6 mice for anesthesia. Then, the mouse liver was exposed through surgery, and a 5# syringe needle (0.5*22 mm) was used to completely penetrate the largest lobe of the liver, causing a wound. After bleeding for 2 s, the wound was completely covered with materials (MCAA, MCC, Cel and Gel). Blank group absorbed blood was left untreated and repeated 5 times for each sample. the bleeding time and blood loss mass were recorded. A tail-amputation model was established by cutting off the C57/BL6 mice tail with surgical scissors, which was an irregular wounds on the body surface [40]. And 25 mice were divided in 5 groups for the untreated group, MCC and MCAA samples, and Gel and Cel for the positive control. Recording the bleeding time and blood loss weight of tail-amputation models. The histocompatibility of MCAA can refer to previous study [40,41]. A dorsal skin trauma with 0.3 cm long on the back of C57/BL6 male mice was fabricated, and about 0.1 mg MCAA was placed in skin and sutured. The same methods were applied to the control group wound, with the only difference being that no material was used for filling. The mice were killed and sampled on the 7th day. After that, the wound epidermis and inflammatory reaction were measured by hematoxylin and eosin (H&E) staining, Masson staining and TNF-α immunohistochemical staining. In addition, all mice were sacrificed and the major organs (heart, liver, spleen, lung and kidney) were harvested for histological staining.

2.13. Statistical analysis

A portion of data was presented by the mean ± standard deviation. Statistical analysis was carried out using one-way analysis of variance (ANOVA). The value of $P < 0.05$ was considered as statistically significant.

3. Results and discussion

To determine the chemical modifications of MCC, the chemical structures of MCC, MCA, and MCAA were analyzed by FT-IR (Fig. 1A). The peaks at 3360 cm^{-1}, 2912 cm^{-1}, 1437 cm^{-1}, and 1376 cm^{-1} in the

infrared spectrum correspond to the stretching vibrations of O–H and C–H bonds, bending vibrations of H–C–H and O–C–H bonds, and the deformation vibration of C–H bonds, respectively [16,42]. These characteristic peaks represented the vibrations of cellulose. There was no significant change in these peaks after surface modification, suggesting that the modification mainly influenced the surface properties and functionalization of cellulose materials, without considerably altering the internal chemical structure. However, it was observed that both MCA and MCAA display an absorption peak at 1740 cm^{-1}, attributable to the carboxyl groups of the grafted AA and CA [43,44]. This peak is emblematic of the carbonyl (C═O) stretching vibration, indicating that carboxylation and grafting reactions of the AA and CA groups took place in the modified MCC samples (Fig. 1B). To quantify the carboxyl groups, those samples were normalized. The intensity of the normalized carboxyl peak at 1745 cm^{-1} for MCA and MCAA was 0.55 ± 0.005 and 0.66 ± 0.004, respectively, and was ascribed to the carboxyl grafting of CA and AA (Fig. 1C). Additionally, as depicted in Fig. S1, compared to the sleek surface of MCC, MCA exhibited a layer of CA shells on its surface. A more pronounced agglomeration of the microcrystals was evident post AA modification. Notably, there was not a marked structural change in MCAA with groups formulated by CA/AA/HCl hydrolysis, in comparison to MCA and MCC. Alterations in the intensities of the C and O atomic signals in the EDS spectra were attributed to CA and AA, respectively (Fig. S2, in the Supporting Information).

As shown in Fig. 1D, the XRD patterns of MCC, MCA and MCAA were depicted. Clearly, all the samples showed the characteristic diffraction peaks at 13.7°, 20.5°, 22.5°, and 33.5°assigning to the ($1\bar{1}0$, 110), (200) and (004) lattice planes, which were typical reflectance of cellulose I [45,46]. There is no obvious change in crystal integrity of cellulose after CA/AA chemical modification. However, the crystallinity of MCAA was increased to 84.59 %, while MCC was 80.77 %, indicating that the crystalline transformation was occurred during the modification of high-temperature and acid environment [47,48]. The graft reactions among carboxyl groups of MCC, MCA and MCAA can be verified by using XPS technique. Compared to MCC, XPS C 1s region from XPS spectra of MCAA was dominated by the peaks of C–C, C–O and C═O, centered at 284.5, 285.9 and 287.3 eV, respectively, indicating the successful grafting of carboxylate group (Fig. S3, supporting information) [31,49,50].

The TGA and DTG curves of MCC, MCA, and MCAA are depicted in Fig. 2C and D, respectively. The onset decomposition temperatures (T_0) and maximum decomposition temperatures (T_{max}) are provided in Table S2. Intriguingly, the T_0 of MCA (338.5 °C) was slightly lower than that of MCC (352.2 °C) due to the presence of unstable carboxyl groups that promote the degradation of glycosidic chains [51,52]. Moreover, the T_{max} of MCAA (472.2 °C) was 22.3 °C higher than that of MCC (449.9 °C), which can be attributed to the enhanced crystallinity of MCAA [16]. Thus, the MCAA synthesized in this study demonstrated superior thermal stability. Beyond that, the carboxyl group content in MCA rose from 4.65 ± 2.0 % to 9.52 ± 1.3 % in the multi-branched MCAA, suggesting a greater prevalence of AA fragments on the MCAA surface (Table S3). These findings further validate that the AA and CA fragments were successfully incorporated onto the cellulose nanocrystals.

Likewise, the hemolysis of RBCs is important for any biomaterials [53]. In this study, the anticoagulant blood was diluted with water and PBS, which were used as positive control and negative control. As shown in Fig. 3A, the hemolysis rates of all samples were less than 5 %, except the Cel groups. This is probably due to the high concentration of Cel. To further show the ability of blood coagulation, the BCI was carried out [54]. The coagulation process of BCI was shown in Fig. 3B. Compared to other commercial hemostatic material (Gel and Cel), the MCAA has a faster clotting rate and lower BCI index. More specifically, BCI of MCAA was 31.3 ± 4.4 %, Gel was 51.8 ± 1.6 % and Cel was 42.7 ± 6.06 % (Fig. 3A). And the MCC had no hemostatic ability.

To understand the biocompatibility of MCAA, we performed cytotoxicity experiments using the NIH3T3 cells. As shown in Fig. 4A–B, cells were viable after 24 h and 72 h of incubation for MCAA, MCC and Gel, with cells surviving in all samples (green). However, the Cel group had fewer cells. Besides, as shown in Fig. 4C–D, the results of cck-8 vitality test showed that Cel group had lower cell viability in comparison to other groups after 24 h and 72 h of incubation. The cell viability of Cel was 77.8 ± 1.8 % in 24 h, while 56.9 ± 4.4 % in 72 h, indicating the cytotoxicity to cells. And 95 % of cells were survived even after 72 of incubation for other groups, suggesting that desirable cytocompatibility of MCAA.

In this work, we established the tail-amputation and liver-injury hemorrhage models in mice to substantiate the macroscopically hemostatic ability of the MCAA. As shown in Fig. 5B, showing the photographs of the tail-amputation models after hemostasis with samples. The MCAA was observed to adhere stably to the wound site without shedding. As shown in Fig. 5C–D, all the samples shortened the bleeding time and reduced the blood loss weight expect MCC. And there were significant differences compared with control group ($P < 0.05$). In concretely, the bleeding time of MCAA was 15 ± 8 s, Gel was 26 ± 4 s, Cel was 14 ± 6 s, which was 75.8 % shorter (MCAA) than that of the control group. For the blood loss weight, MCAA was 0.005 ± 0.0004 g, Gel was 0.007 ± 0.003 g, Cel was 0.006 ± 0.002 g. The results showed that MCAA had stronger hemostatic effect in vivo than other materials.

Visceral hemorrhage is one of the main causes of traumatic death. Herein, to further clarify the hemostatic effect of MCAA in vivo by establishing the liver injury model (Fig. 6A–B). The clotting time and blood lose weight were also measured. Firstly, the blood clotting time of MCC was about 60 ± 27 s, which untreated group was 76 ± 6 s, indicating that there were no significant differences between them. Besides, the bleeding time for the MCAA group was about 17 ± 9 s, and Gel was 34 ± 18 s, which showed a significant reduction to the untreated group (Fig. 6C). As shown in Fig. 6D, the blood loss weight of untreated group and MCC no significant differences, to about 0.14 ± 0.01 g and 0.1 ± 0.01 g, respectively. And the MCAA group was about 0.06 ± 0.01 g, and Gel was about 0.08 ± 0.01 g, demonstrating that the hemostatic effect of MCAA was significant. Through the above results, we believe that the excellent hemostatic effect of MCAA came from CC/AA grafting, and could be applied to the hemorrhage control and irregular wound treatment.

In this work, to explore the interaction of MCAA, whole blood and plasma, the plasma clotting kinetics was carried out. A remarkably faster coagulation rate was observed in MCAA at the beginning of coagulation, compared with that of TCP, Cel and Gel (Fig. 7B), suggesting MCAA could concentrate plasma faster. Besides, there was no obvious change on the pH of blood, indicating a good histocompatibility [55].

To delve deeper into the coagulation mechanism of MCAA, we employed the lactate dehydrogenase (LDH) method to quantitatively assess platelet adhesion to the materials. LDH levels correlate directly with the quantity of platelets [56,57]. LDH levels correlate directly with the quantity of platelets. As illustrated in Fig. S4, the LDH release values for MCAA and MCC were 64.6 ± 2.8 % and 83.8 ± 15.4 %, respectively. These values were notably higher ($p < 0.0001$) than that of Gel group (14.1 ± 1.8 %). This indicated that both MCAA and MCC have more platelets adhering to their surfaces, leading to the formation of platelet aggregates. Intriguingly, MCC did not exhibit hemostatic properties in our prior experiments, likely due to its inherent adsorption characteristics [58]. Furthermore, the carboxyl groups in MCAA intensified platelet aggregation and activation, resulting in the pinnacle LDH levels. In conclusion, the carboxyl group in MCAA seems pivotal in ensuring effective hemostasis.

As illustrated in Fig. S5, the coagulation process primarily encompasses three pathways: extrinsic, intrinsic, and common pathways, which can be evaluated by Prothrombin time (PT) and activated partial thromboplastin time (aPTT) tests. As depicted in Fig. 4D–E, the results indicated that the aPTT values of MCAA group were significantly lower than that of the control group. Specifically, the aPTT values of MCAA

were 15 ± 4 s, Gel registered 27 ± 2 s, Cel was 22 ± 1 s, and control group was 38 ± 4 s, which was 60.5 % shorter than that of the control group. The PT for the MCAA treated plasma also exhibited a decrease. These experimental outcomes suggested that MCAA could stimulate both the intrinsic and extrinsic blood coagulation pathways.

To corroborate this hypothesis, the thrombin-antithrombin complex (TAT), an indicator of thrombin neutralization, was measured [59]. As presented in Fig. S6, in comparison to the control group, the TAT values for MCAA were markedly elevated, signifying that MCAA curtails the clotting time through coagulation factor activation. From above results, it can be confirmed that MCAA would provoke additional recruitment and activation of more platelets when a vessel wall is injured. Then the intrinsic and extrinsic pathways were activated, ultimately promoting hemostasis.

To ascertain its long-term safety in vivo and ensure it does not inflict tissue or significant organ damage, we appraised early inflammatory responses and potential rejection by implanting MCAA subcutaneously into mice for one week (Fig. 8A). As shown in Fig. 8B–C, depict representative histological visuals from H&E and Masson staining for the control and MCAA groups. Post a week-long subcutaneous implantation of MCAA in mice, a modest count of inflammatory cells could be discerned in the progressively contracting wound tissue. Furthermore, the proinflammatory cytokine tumor necrosis factor (TNF)-α is a critical contributor to inflammatory diseases [60]. Herein, using immunocytochemical staining, we demonstrated that the number of TNF-α cells in the MCAA group was similar to that of control group on day 7 (Fig. S7), suggesting that MCAA exhibits a low degree of inflammatory response. Intriguingly, blue collagen was identified surrounding the MCAA, showing that MCAA might have wound repair potential, but this premise demands further investigation. Moreover, juxtaposed with the control group, the H&E staining of major organs revealed no discernible damage (Fig. 8D). These findings bolster the idea that MCAA possesses favorable biocompatibility in vivo and stands as a promising hemostatic agent.

4. Conclusion

In summary, we successfully developed multibranch carboxyl modified cellulose for significant hemorrhage control, and examined its hemostatic efficiency and mechanisms. Our findings indicated that the microstructure, chemical structure, and thermal stability of the material are influenced by the presence of carboxyl groups. In terms of in vitro cytotoxicity and blood compatibility, the MCAA yielded encouraging results. Notably, the MCAA, exhibiting no cytotoxicity, possessed a carboxylic group content of 9.52 %, higher than the citric acid grafted microcrystalline cellulose (MCA) at 4.65 %. This contributed to enhancing the adsorption capacity of platelets and erythrocytes, facilitating a swift hemostatic response. Moreover, an in vitro coagulation study verified that both endogenous and exogenous physiological coagulation pathways are activated by MCAA, influencing the clotting process. Benefitting from the multifaceted hemostatic properties, MCAA demonstrated superior hemostatic performance in vivo liver injury model and tail amputation model studies. Specifically, the clotting times for MCAA (17 s and 15 s) were notably shorter than those of the untreated group (76 s and 62 s) and the gel (34 s and 26 s). Additionally, MCAA exhibited remarkable biocompatibility in vivo trials, offering fresh insights into cellulose-based hemostatic materials designed to mitigate bleeding. Nevertheless, more comprehensive studies are needed to elucidate the mechanisms that enhance the hemostatic effects of multibranch carboxyl-modified cellulose.

CRediT authorship contribution statement

Shengyu Li: Conceptualization, Methodology, Visualization, Formal analysis, Writing - original draft. **Lihong Gong:** Conceptualization, Methodology, Formal analysis. **Jianglin Chen:** Visualization, Formal analysis, Writing - review & editing. **Xijin Wu:** Formal analysis. **Xia Liu:** Funding acquisition. **Huiying Fu:** Conceptualization, Funding acquisition, Project administration. **Qiyang Shou:** Funding acquisition, Resources, Project administration.

Declaration of competing interest

No conflict of interest exits in the submission of this manuscript. This manuscript has not been considered to publish elsewhere.

Data availability

Data will be made available on request.

Acknowledgements

This work was financially supported by the National Natural Science Foundation of China (82304728, 82274175, 82174026, 82004060), Natural Science Foundation of Zhejiang Province (Y23H280029, LY22H280012), Zhejiang Provincial Administration of Traditional Chinese Medicine Co-construction Key Project (GZY-ZJ-KJ-23069), Medical Health Science and Technology project of Zhejiang Province (2022RC220), the Research Project of Zhejiang Chinese Medical University (2023JKJNTZ13) and Zhejiang Provincial Program for the Cultivation of High-level Innovative Health talents.

Appendix A. Supplementary data

Supplementary data to this article can be found online at https://doi.org/10.1016/j.mtbio.2023.100878.

References

[1] B.J. Eastridge, R.L. Mabry, P. Seguin, J. Cantrell, T. Tops, P. Uribe, O. Mallett, T. Zubko, L. Oetjen-Gerdes, T.E. Rasmussen, F.K. Butler, R.S. Kotwal, J.B. Holcomb, C. Wade, H. Champion, M. Lawnick, L. Moores, L.H. Blackbourne, Death on the battlefield (2001-2011): implications for the future of combat casualty care, J. Trauma Acute Care Surg. 73 (6 Suppl 5) (2012) S431–S437, https://doi.org/10.1097/TA.0b013e3182755dcc.

[2] S. Chen, M.A. Carlson, Y.S. Zhang, Y. Hu, J. Xie, Fabrication of injectable and superelastic nanofiber rectangle matrices ("peanuts") and their potential applications in hemostasis, Biomaterials 179 (2018) 46–59, https://doi.org/10.1016/j.biomaterials.2018.06.031.

[3] X.-F. Li, P. Lu, H.-R. Jia, G. Li, B. Zhu, X. Wang, F.-G. Wu, Emerging materials for hemostasis, Coord. Chem. Rev. 475 (2023), https://doi.org/10.1016/j.ccr.2022.214823.

[4] B.S. Kheirabadi, J.E. Mace, I.B. Terrazas, C.G. Fedyk, K.K. Valdez, M.J. MacPhee, D. Beall, J.S. Estep, M.A. Dubick, L.H. Blackbourne, Clot-inducing minerals versus plasma protein dressing for topical treatment of external bleeding in the presence of coagulopathy, J. Trauma 69 (5) (2010) 1062–1072, https://doi.org/10.1097/TA.0b013e3181fa0f21, discussion 1072-1063.

[5] C. Wang, H. Zhou, H. Niu, X. Ma, Y. Yuan, H. Hong, C. Liu, Tannic acid-loaded mesoporous silica for rapid hemostasis and antibacterial activity, Biomater. Sci. 6 (12) (2018) 3318–3331, https://doi.org/10.1039/c8bm00837j.

[6] W. Han, B. Zhou, K. Yang, X. Xiong, S.F. Luan, Y. Wang, Z. Xu, P. Lei, Z.S. Luo, J. Gao, Y.J. Zhan, G.P. Chen, L. Liang, R. Wang, S. Li, H. Xu, Biofilm-inspired adhesive and antibacterial hydrogel with tough tissue integration performance for sealing hemostasis and wound healing, Bioact. Mater. 5 (4) (2020) 768–778, https://doi.org/10.1016/j.bioactmat.2020.05.008.

[7] A. Sen Gupta, A. Girish, K. Jolly, M. de la Fuente, X. Han, M.T. Nieman, A. Recchione, Intravenous nanomedicine for targeted delivery of thrombin to augment hemostasis, Blood 138 (Supplement 1) (2021) 1029, https://doi.org/10.1182/blood-2021-153708, 1029.

[8] I. Urosev, J. Lopez Morales, M.A. Nash, Phase separation of intrinsically disordered protein polymers mechanically stiffens fibrin clots, Adv. Funct. Mater. 30 (51) (2020), https://doi.org/10.1002/adfm.202005245.

[9] S. Li, X. Wu, N. Bai, J. Ni, X. Liu, W. Mao, L. Jin, H. Xiang, H. Fu, Q. Shou, Fabricating oxidized cellulose sponge for hemorrhage control and wound healing, ACS Biomater. Sci. Eng. (2023), https://doi.org/10.1021/acsbiomaterials.3c00018.

[10] K.T. Pomini, D.V. Buchaim, J.C. Andreo, M.P.O. Rosso, B.B. Della Coletta, I.J. S. German, A.C.C. Biguetti, A.L. Shinohara, G.M. Rosa Junior, J.V.T. Cosin Shindo, M.P. Alcalde, M.A.H. Duarte, D. de Bortoli Teixeira, R.L. Buchaim, Fibrin sealant derived from human plasma as a scaffold for bone grafts associated with photobiomodulation therapy, Int. J. Mol. Sci. 20 (7) (2019), https://doi.org/10.3390/ijms20071761.

[11] S. Zhang, J. Li, S. Chen, X. Zhang, J. Ma, J. He, Oxidized cellulose-based hemostatic materials, Carbohydr. Polym. 230 (2020), 115585, https://doi.org/10.1016/j.carbpol.2019.115585.
[12] J.B. Larsen, A.M. Hvas, Thrombin: a pivotal player in hemostasis and beyond, Semin. Thromb. Hemost. 47 (7) (2021) 759–774, https://doi.org/10.1055/s-0041-1727116.
[13] P. Rhee, C. Brown, M. Martin, A. Salim, D. Plurad, D. Green, L. Chambers, D. Demetriades, G. Velmahos, H. Alam, QuikClot use in trauma for hemorrhage control: case series of 103 documented uses, J. Trauma Inj. Infect. Crit. Care 64 (4) (2008) 1093–1099, https://doi.org/10.1097/TA.0b013e31812f6dbc.
[14] H.N. Xu, Y.Y. Tang, X.K. Ouyang, Shear-induced breakup of cellulose nanocrystal aggregates, Langmuir 33 (1) (2017) 235–242, https://doi.org/10.1021/acs.langmuir.6b03807.
[15] A. Basu, J. Hong, N. Ferraz, Hemocompatibility of Ca(2+) -crosslinked nanocellulose hydrogels: toward efficient management of hemostasis, Macromol. Biosci. 17 (11) (2017), https://doi.org/10.1002/mabi.201700236.
[16] M.-L. Song, H.-Y. Yu, L.-M. Chen, J.-Y. Zhu, Y.-Y. Wang, J.-M. Yao, Z. Zou, K. C. Tam, Multibranch strategy to decorate carboxyl groups on cellulose nanocrystals to prepare adsorbent/flocculants and pickering emulsions, Acs Sustain Chem Eng 7 (7) (2019) 6969–6980, https://doi.org/10.1021/acssuschemeng.8b06671.
[17] F. Cheng, C. Liu, H. Li, X. Wei, T. Yan, Y. Wang, Y. Song, J. He, Y. Huang, Carbon nanotube-modified oxidized regenerated cellulose gauzes for hemostatic applications, Carbohydr. Polym. 183 (2018) 246–253, https://doi.org/10.1016/j.carbpol.2017.12.035.
[18] F. Cheng, J.M. He, T.S. Yan, C.Y. Liu, X.J. Wei, J.W. Li, Y.D. Huang, Antibacterial and hemostatic composite gauze of N,O-carboxymethyl chitosan/oxidized regenerated cellulose, RSC Adv. 6 (97) (2016) 94429–94436, https://doi.org/10.1039/c6ra15983d.
[19] R.W. Hutchinson, K. George, D. Johns, L. Craven, G. Zhang, P. Shnoda, Hemostatic efficacy and tissue reaction of oxidized regenerated cellulose hemostats, Cellulose 20 (1) (2013) 537–545, https://doi.org/10.1007/s10570-012-9828-8.
[20] C. Liu, X. Liu, C. Liu, N. Wang, H. Chen, W. Yao, G. Sun, Q. Song, W. Qiao, A highly efficient, in situ wet-adhesive dextran derivative sponge for rapid hemostasis, Biomaterials 205 (2019) 23–37, https://doi.org/10.1016/j.biomaterials.2019.03.016.
[21] W.L. Cheng, J.M. He, Y.D. Wu, C. Song, S.S. Xie, Y.D. Huang, B. Fu, Preparation and characterization of oxidized regenerated cellulose film for hemostasis and the effect of blood on its surface, Cellulose 20 (5) (2013) 2547–2558, https://doi.org/10.1007/s10570-013-0005-5.
[22] L. Bao, Z. Zhang, X. Li, L. Zhang, H. Tian, M. Zhao, T. Ye, W. Cui, Bacteriosynthetic degradable tranexamic acid-functionalized short fibers for inhibiting invisible hemorrhage, Small (2023), e2303615, https://doi.org/10.1002/smll.202303615.
[23] K. Quan, G. Li, L. Tao, Q. Xie, Q. Yuan, X. Wang, Diaminopropionic acid reinforced graphene sponge and its use for hemostasis, ACS Appl. Mater. Interfaces 8 (12) (2016) 7666–7673, https://doi.org/10.1021/acsami.5b12715.
[24] F. Cheng, C. Liu, X. Wei, T. Yan, H. Li, J. He, Y. Huang, Preparation and characterization of 2,2,6,6-Tetramethylpiperidine-1-oxyl (TEMPO)-Oxidized cellulose nanocrystal/alginate biodegradable composite dressing for hemostasis applications, Acs Sustain Chem Eng 5 (5) (2017) 3819–3828, https://doi.org/10.1021/acssuschemeng.6b02849.
[25] S. Devarajan, M. Muthuchamy, A. Muthukumar, G. Venkateshwarapuram Rengaswami, Development of oxidized cellulose fabrics for hemostat applications, Mater. Lett. 308 (2022), https://doi.org/10.1016/j.matlet.2021.131160.
[26] S.N. Ye, H.Y. Yu, D.C. Wang, J.Y. Zhu, J.P. Gu, Green acid-free one-step hydrothermal ammonium persulfate oxidation of viscose fiber wastes to obtain carboxylated spherical cellulose nanocrystals for oil/water Pickering emulsion, Cellulose 25 (9) (2018) 5139–5155, https://doi.org/10.1007/s10570-018-1917-x.
[27] T. Suopajarvi, H. Liimatainen, O. Hormi, J. Niinimaki, Coagulation-flocculation treatment of municipal wastewater based on anionized nanocelluloses, Chem. Eng. J. 231 (2013) 59–67, https://doi.org/10.1016/j.cej.2013.07.010.
[28] D.-Z.Z. Hou-Yong Yu, Fang-Fang Lu, Juming Yao, New approach for single-step extraction of carboxylated cellulose nanocrystals for their use as adsorbents and flocculants, ACS Sustainable Chem. Eng. 4 (5) (2016), https://doi.org/10.1021/acssuschemeng.6b00126.
[29] C. Li, Z. Hou, P. Li, G. Zhang, L. Bai, W. Wang, H. Chen, H. Yang, L. Yang, Phytic acid-assist for self-healing nanocomposite hydrogels with surface functionalization of cellulose nanocrystals via SI-AGET ATRP, Cellulose 30 (2) (2022) 1087–1102, https://doi.org/10.1007/s10570-022-04936-5.
[30] T. Willhammar, K. Daicho, D.N. Johnstone, K. Kobayashi, Y. Liu, P.A. Midgley, L. Bergstrom, T. Saito, Local crystallinity in twisted cellulose nanofibers, ACS Nano 15 (2) (2021) 2730–2737, https://doi.org/10.1021/acsnano.0c08295.
[31] C.Y.H.Y.J. Yao, One-step extraction and functionalization of cellulose nanospheres from lyocell fibers with cellulose II crystal structure, Cellulose 22 (2015) 3773, https://doi.org/10.1007/s10570-015-0761-5.
[32] H. Han, A. Li, M. Zhu, S. Hu, J. Xu, Z. Xiong, Q. Ren, Y. Wang, L. Jiang, S. Su, J. Xiang, Heavy tar evolution characteristics during advanced sludge pyrolysis and biomass gasification integrated process, Sci. Total Environ. 853 (2022), 158107, https://doi.org/10.1016/j.scitotenv.2022.158107.
[33] Z. Zhang, M. Zhu, D. Zhang, A Thermogravimetric study of the characteristics of pyrolysis of cellulose isolated from selected biomass, Appl. Energy 220 (2018) 87–93, https://doi.org/10.1016/j.apenergy.2018.03.057.
[34] H. Wu, W. Lu, Y. Chen, P. Zhang, X. Cheng, Application of Boehm titration for the quantitative measurement of soot oxygen functional groups, Energy Fuel. 34 (6) (2020) 7363–7372, https://doi.org/10.1021/acs.energyfuels.0c00904.
[35] C. Wang, H. Niu, X. Ma, H. Hong, Y. Yuan, C. Liu, Injectable Bioinspired, Quaternized hydroxyethyl cellulose composite hydrogel coordinated by mesocellular silica foam for rapid, noncompressible hemostasis and wound healing, ACS Appl. Mater. Interfaces 11 (38) (2019) 34595–34608, https://doi.org/10.1021/acsami.9b08799.
[36] H. Cheng, X. Pan, Z. Shi, X. Huang, Q. Zhong, H. Liu, Y. Chen, Q. Lian, J. Wang, Z. Shi, Chitin/corn stalk pith sponge stimulated hemostasis with erythrocyte absorption, platelet activation, and Ca(2+)-binding capabilities, Carbohydr. Polym. 284 (2022), 118953, https://doi.org/10.1016/j.carbpol.2021.118953.
[37] J. Liu, X. Zhou, Y. Zhang, W. Zhu, A. Wang, M. Xu, S. Zhuang, Rapid hemostasis and excellent antibacterial cerium-containing mesoporous bioactive glass/chitosan composite sponge for hemostatic material, Mater. Today Chem. 23 (2022), https://doi.org/10.1016/j.mtchem.2021.100735.
[38] F. Song, Y. Kong, C. Shao, Y. Cheng, J. Lu, Y. Tao, J. Du, H. Wang, Chitosan-based multifunctional flexible hemostatic bio-hydrogel, Acta Biomater. 136 (2021) 170–183, https://doi.org/10.1016/j.actbio.2021.09.056.
[39] S.S. Biranje, P.V. Madiwale, K.C. Patankar, R. Chhabra, P. Dandekar-Jain, R. V. Adivarekar, Hemostasis and anti-necrotic activity of wound-healing dressing containing chitosan nanoparticles, Int. J. Biol. Macromol. 121 (2019) 936–946, https://doi.org/10.1016/j.ijbiomac.2018.10.125.
[40] C. Zheng, J. Liu, Q. Bai, Y. Quan, Z. Li, W. Chen, Q. Gao, Y. Zhang, T. Lu, Preparation and hemostatic mechanism of bioactive glass-based membrane-like structure camouflage composite particles, Mater. Des. 223 (2022), https://doi.org/10.1016/j.matdes.2022.111116.
[41] W. Liu, M. Wang, W. Cheng, W. Niu, M. Chen, M. Luo, C. Xie, T. Leng, L. Zhang, B. Lei, Bioactive antiinflammatory antibacterial hemostatic citrate-based dressing with macrophage polarization regulation for accelerating wound healing and hair follicle neogenesis, Bioact. Mater. 6 (3) (2021) 721–728, https://doi.org/10.1016/j.bioactmat.2020.09.008.
[42] Y. Liu, X. Lv, J. Bao, J. Xie, X. Tang, J. Che, Y. Ma, J. Tong, Characterization of silane treated and untreated natural cellulosic fibre from corn stalk waste as potential reinforcement in polymer composites, Carbohydr. Polym. 218 (2019) 179–187, https://doi.org/10.1016/j.carbpol.2019.04.088.
[43] A. Boujemaoui, C. Cobo Sanchez, J. Engstrom, C. Bruce, L. Fogelstrom, A. Carlmark, E. Malmstrom, Polycaprolactone nanocomposites reinforced with cellulose nanocrystals surface-modified via covalent grafting or physisorption: a comparative study, ACS Appl. Mater. Interfaces 9 (40) (2017) 35305–35318, https://doi.org/10.1021/acsami.7b09009.
[44] C.F. Yan, H.Y. Yu, J.M. Yao, One-step extraction and functionalization of cellulose nanospheres from lyocell fibers with cellulose II crystal structure, Cellulose 22 (6) (2015) 3773–3788, https://doi.org/10.1007/s10570-015-0761-5.
[45] J. Henschen, D.F. Li, M. Ek, Preparation of cellulose nanomaterials via cellulose oxalates, Carbohydr. Polym. 213 (2019) 208–216, https://doi.org/10.1016/j.carbpol.2019.02.056.
[46] L.K. Kian, N. Saba, M. Jawaid, H. Fouad, Characterization of microcrystalline cellulose extracted from olive fiber, Int. J. Biol. Macromol. 156 (2020) 347–353, https://doi.org/10.1016/j.ijbiomac.2020.04.015.
[47] H.Y. Bian, L.H. Chen, H.Q. Dai, J.Y. Zhu, Integrated production of lignin containing cellulose nanocrystals (LCNC) and nanofibrils (LCNF) using an easily recyclable di-carboxylic acid, Carbohydr. Polym. 167 (2017) 167–176, https://doi.org/10.1016/j.carbpol.2017.03.050.
[48] S. Liu, Q. Zhang, S. Gou, L. Zhang, Z. Wang, Esterification of cellulose using carboxylic acid-based deep eutectic solvents to produce high-yield cellulose nanofibers, Carbohydr. Polym. 251 (2021), 117018, https://doi.org/10.1016/j.carbpol.2020.117018.
[49] Y.C. Luo, T. Song, H. Ji, H.S. Qi, Z.Y. Xiang, H.P. Xiong, Y. Cen, G. Chen, T.T. Han, A. Pranovich, Preliminary investigations of the mechanisms involved in the ultrasonication-assisted production of carboxylic cellulose nanocrystals with different structural carboxylic acids, Acs Sustain Chem Eng 9 (12) (2021) 4531–4542, https://doi.org/10.1021/acssuschemeng.0c08929.
[50] X. Chen, X. Wang, D. Fang, A review on C1s XPS-spectra for some kinds of carbon materials, Fullerenes, Nanotub. Carbon Nanostruct. 28 (12) (2020) 1048–1058, https://doi.org/10.1080/1536383x.2020.1794851.
[51] N. Yousefi, K.K.W. Wong, Z. Hosseinidoust, H.O. Sorensen, S. Bruns, Y. Zheng, N. Tufenkji, Hierarchically porous, ultra-strong reduced graphene oxide-cellulose nanocrystal sponges for exceptional adsorption of water contaminants, Nanoscale 10 (15) (2018) 7171–7184, https://doi.org/10.1039/c7nr09037d.
[52] P.R. Sharma, A.J. Varma, Thermal stability of cellulose and their nanoparticles: effect of incremental increases in carboxyl and aldehyde groups, Carbohydr. Polym. 114 (2014) 339–343, https://doi.org/10.1016/j.carbpol.2014.08.032.
[53] Z. Tang, H. He, L. Zhu, Z. Liu, J. Yang, G. Qin, J. Wu, Y. Tang, D. Zhang, Q. Chen, J. Zheng, A general protein unfolding-chemical coupling strategy for pure protein hydrogels with mechanically strong and multifunctional properties, Adv. Sci. 9 (5) (2022), e2102557, https://doi.org/10.1002/advs.202102557.
[54] J. Jimenez-Martin, K. Las Heras, A. Etxabide, J. Uranga, K. de la Caba, P. Guerrero, M. Igartua, E. Santos-Vizcaino, R.M. Hernandez, Green hemostatic sponge-like scaffold composed of soy protein and chitin for the treatment of epistaxis, Mater Today Bio 15 (2022), 100273, https://doi.org/10.1016/j.mtbio.2022.100273.
[55] C.L. Dai, Y. Yuan, C.S. Liu, J. Wei, H. Hong, X.S. Li, X.H. Pan, Degradable, antibacterial silver exchanged mesoporous silica spheres for hemorrhage control, Biomaterials 30 (29) (2009) 5364–5375, https://doi.org/10.1016/j.biomaterials.2009.06.052.
[56] I. Jardin, J.J. Lopez, J.A. Pariente, G.M. Salido, J.A. Rosado, Intracellular calcium release from human platelets: different messengers for multiple stores, Trends Cardiovasc. Med. 18 (2) (2008) 57–61, https://doi.org/10.1016/j.tcm.2007.12.004.

[57] Z. Chen, X. Yao, L. Liu, J. Guan, M. Liu, Z. Li, J. Yang, S. Huang, J. Wu, F. Tian, M. Jing, Blood coagulation evaluation of N-alkylated chitosan, Carbohydr. Polym. 173 (2017) 259–268, https://doi.org/10.1016/j.carbpol.2017.05.085.
[58] B.G. Cho, S.B. Mun, C.R. Lim, S.B. Kang, C.W. Cho, Y.S. Yun, Adsorption modeling of microcrystalline cellulose for pharmaceutical-based micropollutants, J. Hazard Mater. 426 (2022), 128087, https://doi.org/10.1016/j.jhazmat.2021.128087.
[59] S. Pourshahrestani, E. Zeimaran, N.A. Kadri, N. Gargiulo, H.M. Jindal, S.V. Naveen, S.D. Sekaran, T. Kamarul, M.R. Towler, Potency and cytotoxicity of a novel gallium-containing mesoporous bioactive glass/chitosan composite scaffold as hemostatic agents, Acs Appl Mater Inter 9 (37) (2017) 31381–31392, https://doi.org/10.1021/acsami.7b07769.
[60] Y. Wang, Y. Wu, L. Long, L. Yang, D. Fu, C. Hu, Q. Kong, Y. Wang, Inflammation-responsive drug-loaded hydrogels with sequential hemostasis, antibacterial, and anti-inflammatory behavior for chronically infected diabetic wound treatment, ACS Appl. Mater. Interfaces 13 (28) (2021) 33584–33599, https://doi.org/10.1021/acsami.1c09889.